Effect of Reaction Time on Microwave Absorption Properties of Fe_3O_4 Hollow Spheres Synthesized via Ostwald Ripening

Wei Huang, Yujiang Wang *, Shicheng Wei *, Bo Wang, Yi Liang, Yuwei Huang and Binshi Xu

National Key Laboratory for Remanufacturing, Army Academy of Armored Forces, Beijing 100072, China

* Correspondence: hitwyj@126.com (Y.W.); wsc33333@163.com (S.W.); Tel.: +86-010-66718541 (Y.W.); +86-010-66719083 (S.W.)

check for updates

Abstract: Hollow magnetic structures have great potential to be used in the microwave absorbing field. Herein, Fe_3O_4 hollow spheres with different levels of hollowness were synthesized by the hydrothermal method under Ostwald ripening effect. In addition to their microstructures, the microwave absorption properties of such spheres were investigated. The results show that the grain size and hollowness of Fe_3O_4 hollow spheres both increase as the reaction time increases. With increasing hollowness, the attenuation ability of electromagnetic wave of Fe_3O_4 spheres increases first and then decreases, finally increases sharply after the spheres break down. Samples with strong attenuation ability can achieve good impedance matching, which it does preferentially as the absorber thickness increases. Fe_3O_4 hollow spheres show the best microwave absorption performance when the reaction time is 24 h. The minimum reflection loss ($R_{L\ (min)}$) can reach −40 dB, while the thickness is only 3.2 mm.

Keywords: Fe_3O_4; hollow sphere; Ostwald ripening; attenuation ability; impedance matching; microwave absorption

1. Introduction

It is well known that the structure of materials plays an important role in their thermo-mechanical behavior and transport properties. Hollow structures have shown great application prospects in lithium batteries, super capacitors, drug transport, biomedicine, gas sensors and other fields due to their advantages of large specific surface area and low density [1–6]. Template methods and template-free methods are usually used to construct hollow structures. Template-free methods usually adopt some special mechanisms, such as the Ostwald ripening effect [7], the Kendall effect [8], the current displacement effect [9], etc. Compared with template methods, template-free methods are more flexible and convenient. In recent years, with the wide application of communication technology and electromagnetic equipment in GHz, electromagnetic radiation has resulted in unprecedented pollution and seriously endangered human health [10–13]. To solve this problem, a lot of efforts have been directed towards the research and development of microwave absorbing materials (MAMs) [14,15]. As a traditional microwave absorbing material, Fe_3O_4 has high saturation magnetization and Curie temperature at high temperature (585 °C). This stable and excellent magnetic property has attracted many scholars' attention. However, the high density of Fe_3O_4 limits its further use as a MAM [16].

Fortunately, many studies have shown that hollowing of Fe_3O_4 is an effective way to reduce material weight, produce special morphological effects and improve electromagnetic properties [17–19]. For example, Li et al. [20] prepared hollow Fe_3O_4 spheres with a diameter of 450 nm, a wall thickness of 80 nm and a density of 3.28 g/cm^3 by solvothermal method, which was nearly 27% lower than the

corresponding solid Fe_3O_4. Sui et al. [21] used the improved solvothermal method to control the size of Fe_3O_4 hollow spheres, and synthesized hollow spheres with diameters of 200–1000 nm and wall thicknesses of 35–280 nm. Xu et al. [22] prepared hollow Fe_3O_4 spheres with a diameter of 525 nm by thermal solvent method. When the filling mass is 60% and the thickness is 3 mm, the minimum reflection loss can reach −15.8 dB. The above research shows that the Fe_3O_4 hollow spheres with low density have very good application prospects in the field of microwave absorption, and that it is feasible to adjust the electromagnetic characteristics of Fe_3O_4 hollow spheres by morphology control. However, the relationship between the morphology of Fe_3O_4 hollow spheres and the microwave absorption characteristics remains to be further studied.

In the present work, Fe_3O_4 hollow spheres with different levels of hollowness were prepared by Ostwald ripening mechanism. The variation of the morphology of Fe_3O_4 hollow spheres under the Ostwald ripening mechanism was studied. The relationships among solvothermal reaction time, structure of Fe_3O_4 hollow spheres and electromagnetic properties were discussed.

2. Experimental

A typical preparation of hollow Fe_3O_4 was carried out as follows: 10 g Polyvinylpyrrolidone (PVP), 9 g $FeCl_3 \cdot 6H_2O$ and 36 g urea were dissolved in 400 mL ethylene glycol, and stirred for 0.5 h by electric mixer to get a deep orange transparent homogenous solution. Then, they were put into a 500 mL stainless-steel autoclave with teflon-lining, and kept at 200 °C for 8 h, 12 h, 16 h, 20 h and 24 h, respectively. After the reaction, all the reaction products were washed with water and alcohol for three times to remove the unreacted. Finally, the reaction products were collected by a magnet and dried in vacuum at 60 °C for 10 h. The code numbers of the sample at 8 h, 12 h, 16 h, 20 h and 24 h were marked as S1, S2, S3, S4 and S5, respectively.

The morphology and structure of Fe_3O_4 hollow microspheres were analyzed by a field emission scanning electron microscope (FESEM, JEOLJSM-6500F, Eindhoven, Holland), transmission electron microscopy (TEM, Tecnai-TF20, Oberkochen, German), and X-ray diffractometer (XRD, Japan Rigaku D/MAX-cA) using a CuKa radiation ($\lambda = 1.5406$ Å). The magnetostatic properties were characterized by vibrating sample magnetometer (VSM, BHV-55). The permeability and permittivity of samples in the frequency range 2–18 GHz were tested by a vector network analyzer (VNA, N5242A, Agilent) for simulation of reflection loss. Composite sample were realized as follows: the wax was melted at 80 °C and mixed with the Fe_3O_4 powder homogeneously. The mixture was moved into a toroidal mold ($\Phi_{in} = 3.04$ mm, $\Phi_{out} = 7$ mm). The test software (Agilent, Santa Clara, CA, USA) is 85071 and the calibration part is 85050D. Before the test, the permittivity of air was measured as an evaluation of calibration effect.

3. Results and Discussion

XRD results of Fe_3O_4 with different reaction times are shown in Figure 1. The diffraction peaks of the samples correspond well to face-centered magnetite Fe_3O_4 (JCPDS Card No. 99-0073), which indicates that the synthesized products have high purity. The diffraction peak intensities increase obviously as the reaction time increases. This means that the samples' crystallinity is improved as the reaction time increases. According to the calculation results of the Scherrer formula ($D = K\gamma/B\cos\theta$), the grain size of the sample at 8 h, 12 h, 16 h, 20 h and 24 h is 25.89 nm, 30.54 nm, 38.28 nm, 41.55 nm and 48.29 nm, respectively. The results show that the grain size increases as the reaction time increases. To further identify the purity of Fe_3O_4, RedOx tiration (potassium dichromate) was used. Table 1 calculates $n(Fe^{2+}):n(Fe^{3+})$, $Fe_\sigma O_4$ (σ-nonstoichiometric) and Oxidation rate, respectively. Although Fe_3O_4 may be oxidized during the experiment, the results in Table 1 show that their oxidation rates are below 10%, which indicates that the purity of Fe_3O_4 phase in the product is very high.
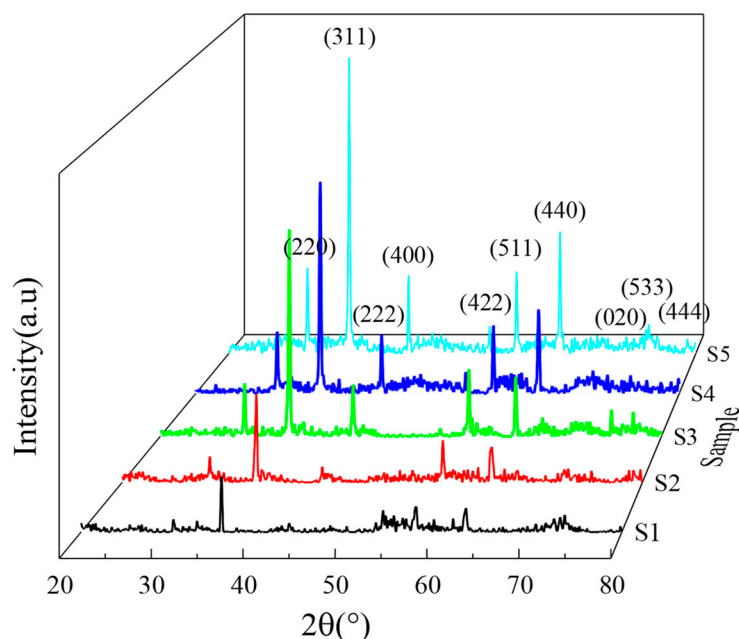
Figure 1. XRD patterns of Fe_3O_4 samples with different reaction times.

Table 1. Purity analysis of Fe_3O_4 by RedOx titration: $n(Fe^{2+}):n(Fe^{3+})$, $Fe_\sigma O_4$ (σ-nonstoichiometric) and oxidation rate.

Sample	$n(Fe^{2+}):n(Fe^{3+})$	$Fe_\sigma O_4$	Oxidation Rate
S1	0.449	$Fe_{2.974}O_4$	7.21 %
S2	0.463	$Fe_{2.982}O_4$	5.27 %
S3	0.455	$Fe_{2.977}O_4$	6.38 %
S4	0.459	$Fe_{2.979}O_4$	5.82 %
S5	0.453	$Fe_{2.976}O_4$	6.65 %

To observe the morphology and internal structure of the samples, SEM and TEM analyses were carried out, and the results are illustrated in Figure 2. The prepared Fe_3O_4 spheres exhibit good dispersion and no agglomeration. As shown in the SEM images from Figure 2a–e, it can be seen that the surface of the Fe_3O_4 sphere is composed of many Fe_3O_4 grains, which shows the self-assembly effect of Ostwald ripening mechanism. Similar results can be seen from the TEM images, Figure 2f–j. In addition, the hollowness of Fe_3O_4 sphere increases gradually as the reaction time increases. The hollow size of Fe_3O_4 increases to breaking point as the reaction time reaches 24 h (S5). It is worth mentioning that although the formation of Fe_3O_4 hollow spheres reflects the typical Ostwald ripening phenomenon, the size of Fe_3O_4 spheres does not increase significantly during the whole reaction process. As can be seen from Figure 2k, the sizes of the Fe_3O_4 hollow spheres are mainly around 500 nm before they are broken. This may be due to the higher PVP concentration, which restricts the growth of Fe_3O_4 spheres during Ostwald ripening process [23].
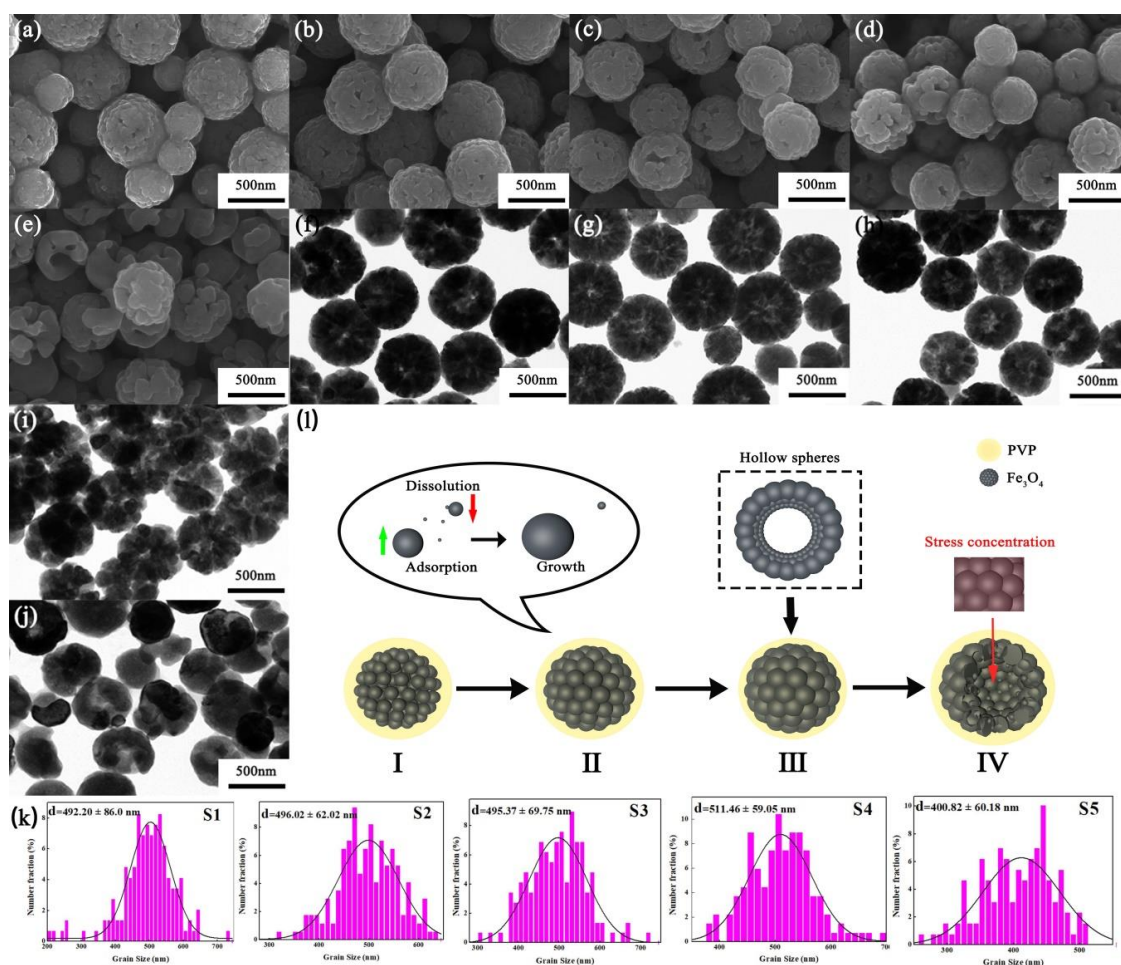
Figure 2. SEM of samples: (**a**) S1, (**b**) S2, (**c**) S3, (**d**) S4, (**e**) S5; TEM of samples: (**f**) S1, (**g**) S2, (**h**) S3, (**i**) S4, (**j**) S5; (**k**) Size distribution of Fe$_3$O$_4$ samples; (**l**) Schematic diagram of the formation process of Fe$_3$O$_4$ by Ostwald ripening.

Based on the results of SEM and TEM images, the formation process of Fe$_3$O$_4$ in this study can be explained as shown in Figure 2l. Firstly, iron ions and oxygen ions react continuously to form grains dispersed in solution under high temperature and pressure. These grains are extremely unstable due to the high surface free energy. To reduce the surface free energy, they will be aggregated into larger loose microspheres, which are the embryonic form of Fe$_3$O$_4$ spheres, as illustrated in Figure 2l-I. From Figure 2l-II to III, with the prolongation of reaction time, the primary grains in outer layer of the microspheres contact with the solution sufficiently, and the absorption rate of iron and oxygen ions from the solution is faster, resulting in the larger grain size than the internal grain size. Then, the internal grains dissolve into the surrounding medium gradually, and re-precipitate on the surface of the external grains due to the higher surface free energy of internal grains. Therefore, the external grains grow further, leading to the formation of Fe$_3$O$_4$ spheres with hollow structure. In addition, there is residual stress in the external grains due to the continuous growth of Fe$_3$O$_4$ grains and the restraint of high PVP concentration. Excessive residual stress leads to the cracks at grain boundaries, resulting in crystal rupture, and the rupture of Fe$_3$O$_4$ spheres ultimately, as shown in Figure 2l-IV.

Figure 3 is a comparison diagram of hysteresis loops for Fe$_3$O$_4$ samples at different reaction time. The saturation magnetization and coercivity of Fe$_3$O$_4$ samples are shown in Table 2. The morphology of Fe$_3$O$_4$ has a significant effect on its magnetic properties. As the reaction time is prolonged, the defects of the sample decrease, the crystallinity is improved, and the super-exchange effect of the Fe–O–Fe bond is enhanced, resulting in a higher saturation magnetization [24]. However, the saturation magnetization of Fe$_3$O$_4$ is woken up as the reaction time is in the range of 12–24 h, which may be due to

the hollow structure reducing the magnetic coupling between the Fe_3O_4 grains. The hollow structure may have a certain strengthening effect on the coercive force of Fe_3O_4, which is manifested in the increase in the coercive force of the Fe_3O_4 sphere at higher hollowness, and which suddenly decreases when the hollow sphere is broken. The report [25] shows that the critical size of superparamagnetism of Fe_3O_4 nanoparticles is 25 nm. Fe_3O_4 grains prepared in this paper are generally larger than this value, thus showing so it shows ferromagnetism.
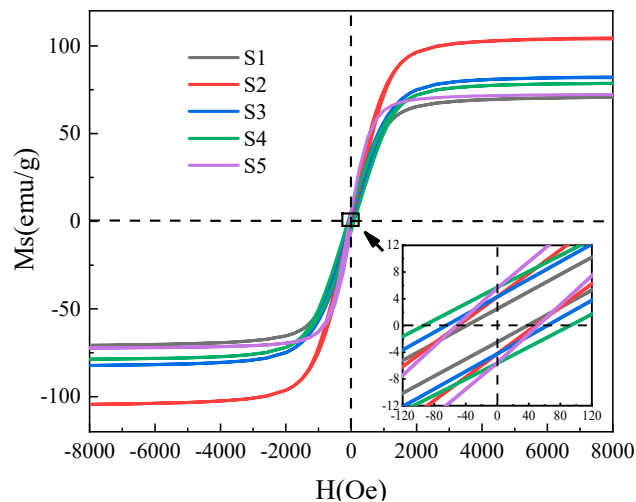

Figure 3. Magnetic hysteresis loop of Fe_3O_4 hollow spheres at room temperature.

Table 2. Magnetic properties of Fe_3O_4 hollow spheres at different reaction time.

Sample	Saturation Magnetization (emu/g)	Coercive Force (H/Oe)
S1	70.64	74.7
S2	103.93	98.8
S3	81.83	129.7
S4	78.55	188.8
S5	72.27	101.4

The frequency dependence of complex permittivity ($\varepsilon_r = \varepsilon' - j\varepsilon''$), dielectric loss tangent and Cole-Cole semicircle of samples in the range of 2–18 GHz are illustrated in Figure 4. Generally speaking, the real part of permittivity ε' is produced by various displacement polarization within the material, it represents the energy storage term of the material. The imaginary part of permittivity, ε'', is produced by various relaxation polarizations caused by steering polarization in the material, it cannot keep up with the change of external high frequency electric field, and represents the loss term of material. As shown in Figure 4a,b, the complex permittivity of Fe_3O_4 hollow spheres with different morphologies varies significantly with the increase of reaction time. The variation ranges of real and imaginary parts of complex permittivity are 6.1–11.8 and 0.2–1.5, respectively. The dielectric properties of different samples vary greatly and show no obvious regularity, which is related to the complex variation of polarization and conductivity affected by the grain size of Fe_3O_4 and the state of dispersion and aggregation.
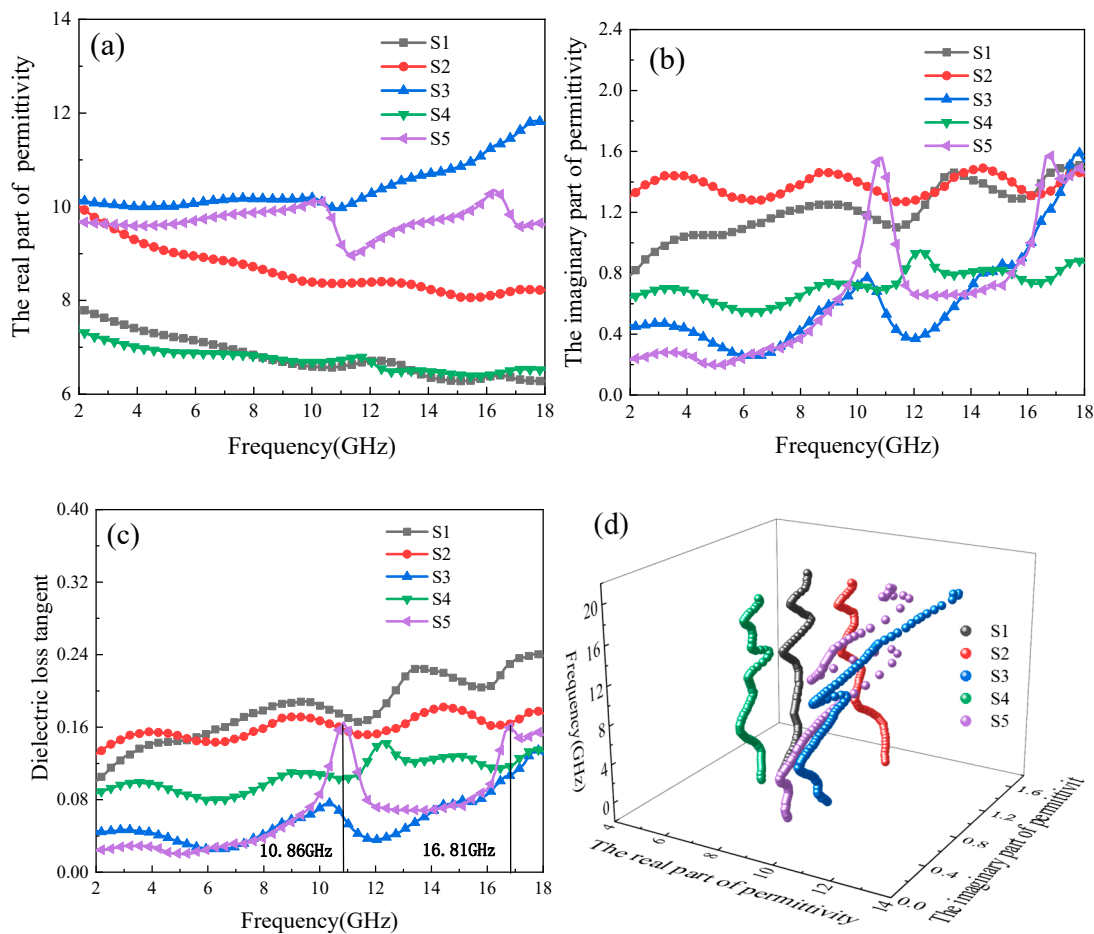
Figure 4. (**a**) The real part of permittivity, (**b**) the imaginary part of permittivity, (**c**) dielectric loss tangent, and (**d**) Cole-Cole curves of Fe_3O_4 in the range of 2–18 GHz.

The dielectric loss tangent (tan $\delta_E = \varepsilon''/\varepsilon'$) reflects the dielectric loss ability of material. Tan δ_E of Fe_3O_4 samples at different time are shown in Figure 4c. ε' changes gently with frequency; the trend of tan δ_E is similar to ε''. Tan δ_E decreases with the prolongation of reaction time (S1–S3) before the rupture of Fe_3O_4 spheres, and increases slightly as the reaction time reaches 20 h (S4). There are two obvious loss peaks in tan δ_E curve with frequency after the rupture of Fe_3O_4 spheres (S5), at 10.86 GHz and 16.82 GHz, respectively. The appearance of the loss peak increases the dielectric loss capacity of S5 at this frequency greatly. According to Debye relaxation theory, the real and imaginary parts of complex permittivity can be transformed into the following form [26]:

$$\varepsilon_r = \varepsilon_\infty + \frac{\varepsilon_s - \varepsilon_\infty}{1 + j2\pi f\tau} = \varepsilon' - j\varepsilon'' \tag{1}$$

In Formula (1), f is the frequency, ε_∞ and ε_s are relative dielectric permittivity at the high-frequency limit and static dielectric permittivity, respectively, and τ is the relaxation time. Therefore, ε' and ε'' can be further transformed:

$$\varepsilon' = \varepsilon_\infty + \frac{\varepsilon_s - \varepsilon_\infty}{1 + (2\pi f)^2\tau^2} \tag{2}$$

$$\varepsilon'' = \frac{2\pi f\tau(\varepsilon_s - \varepsilon_\infty)}{1 + (2\pi f)^2\tau^2} \tag{3}$$

According to Formulas (2) and (3), the relationship between ε' and ε'' can be further deduced:

$$\left(\varepsilon' - \frac{\varepsilon_s + \varepsilon_\infty}{2}\right)^2 + (\varepsilon'')^2 = \left(\frac{\varepsilon_s - \varepsilon_\infty}{2}\right)^2 \tag{4}$$

According to Formula (4). If the polarization of the permittivity is caused by Debye relaxation process, it will be shown as a Cole-Cole semicircle. Based on the above theory, 3D illustration of Cole-Cole curves is made as shown in Figure 4d. First, for S1–S4, no Debye semicircles exist, and the Cole-Cole curves are just twisted spirals. Even for S5, it is not an ideal Debye semicircle. According to Formulas (2) and (3), if the dielectric spectrum satisfies the Debye relaxation equation, the maximum value of ε'' appears and $\varepsilon'' = (\varepsilon_s - \varepsilon_\infty)/2$ when $2\pi f = \tau^{-1}$. However, the ε' of S5 is maintained at about 10 initially, then decreases to 8.9 from 10.3 to 11.4 GHz, resulting in a value that corresponds to a loss peak of ε'' (10.86 GHz). Simply estimated, the maximum value of the loss peak is much larger than that of $(\varepsilon_s - \varepsilon_\infty)/2$, indicating that the dielectric behavior is not a typical Debye relaxation. This behavior may correspond to a resonance process similar to dielectric relaxation. Overall, we consider that the dielectric loss of Fe_3O_4 is not Debye relaxation, but resonant dielectric response.

Figure 5 displays the frequency dependence of complex permeability ($\mu_r = \mu' - j\mu''$), magnetic loss tangent and C_0 of samples in the range of 2–18 GHz. From Figure 5a,b, it can be seen that real part of permeability (μ') and imaginary part of permeability (μ'') curves exhibit a similar trend, decreasing first and then remaining stable. This indicates that the magnetic loss ability of Fe_3O_4 is mainly reflected in the S band (2–4 GHz) and C band (4–8 GHz), and Ostwald ripening has less effect on the magnetic properties than on the dielectric properties of Fe_3O_4. Similarly to dielectric loss, the magnetic loss tangent ($\tan \delta_M = \mu''/\mu'$) reflects the magnetic loss ability of materials, and $\tan \delta_M$ can also be observed in Figure 5c. The results show that there is a loss peak at the tested frequency of $\tan \delta_M$, at which is much larger than that of $\tan \delta_E$. $\mathrm{Tan}\, \delta_M$ decreases slowly and finally approaches to $\tan \delta_E$ as the frequency increases. Therefore, it can be judged that the loss mechanism of Fe_3O_4 is mainly magnetic loss. For ferrite materials, magnetic loss is usually caused by hysteresis loss, eddy current loss, domain wall displacement and natural resonance. However, hysteresis loss can be neglected in the case of weak applied electric field, and domain wall displacement only occurs in the MHz range, so the magnetic loss mechanism in Fe_3O_4 is generally related to eddy current loss and natural resonance. Material thickness (d) and conductivity (σ) are two main factors affecting eddy current loss, which can be expressed as follows [27]:

$$C_0 = \mu'' (\mu')^{-2} f^{-1} = \frac{2}{3} \pi \mu_0 d^2 \sigma \tag{5}$$

If the magnetic loss is caused entirely by the eddy current loss, the right side of Equation (5) is constant, so no the variation of C_0 with frequency should be revealed in a constant. In other words, the eddy current loss should be dominant in the frequency range of relatively stable and small fluctuations. As shown in Figure 5d, C_0 curves of Fe_3O_4 fluctuate greatly at low frequencies and tend to be stable at the middle and high frequencies, indicating that the magnetic loss should be caused by natural resonance at low frequency, and as the frequency increases, it gradually changes into eddy current loss. Combined with Figure 5c, the corresponding frequencies of loss peaks caused by natural resonance at low frequencies are 2.86 GHz (S1), 4.12 GHz (S2), 4.16 GHz (S3), 3.77 GHz (S4) and 4.55 GHz (S5), respectively. The difference of natural resonance frequencies between different samples is caused by the effective anisotropy field of magneto-crystals with different morphologies of Fe_3O_4 [28]. In addition, C_0 approaches zero at the middle and high frequencies, indicating that the eddy current loss is very weak. This is consistent with the weak magnetic loss at the corresponding frequency in Figure 5c. It is noteworthy that there is also a loss peak at 12 GHz in S1, which is caused by exchange resonance. A relevant report shows that there is exchange resonance as the grain size of Fe_3O_4 is about 10 nm [29]. In addition, S1 is the early formation stage of the Fe_3O_4 hollow spheres; there are some grains about 10 nm in size, so the speculation of exchange resonance in S1 is valid.
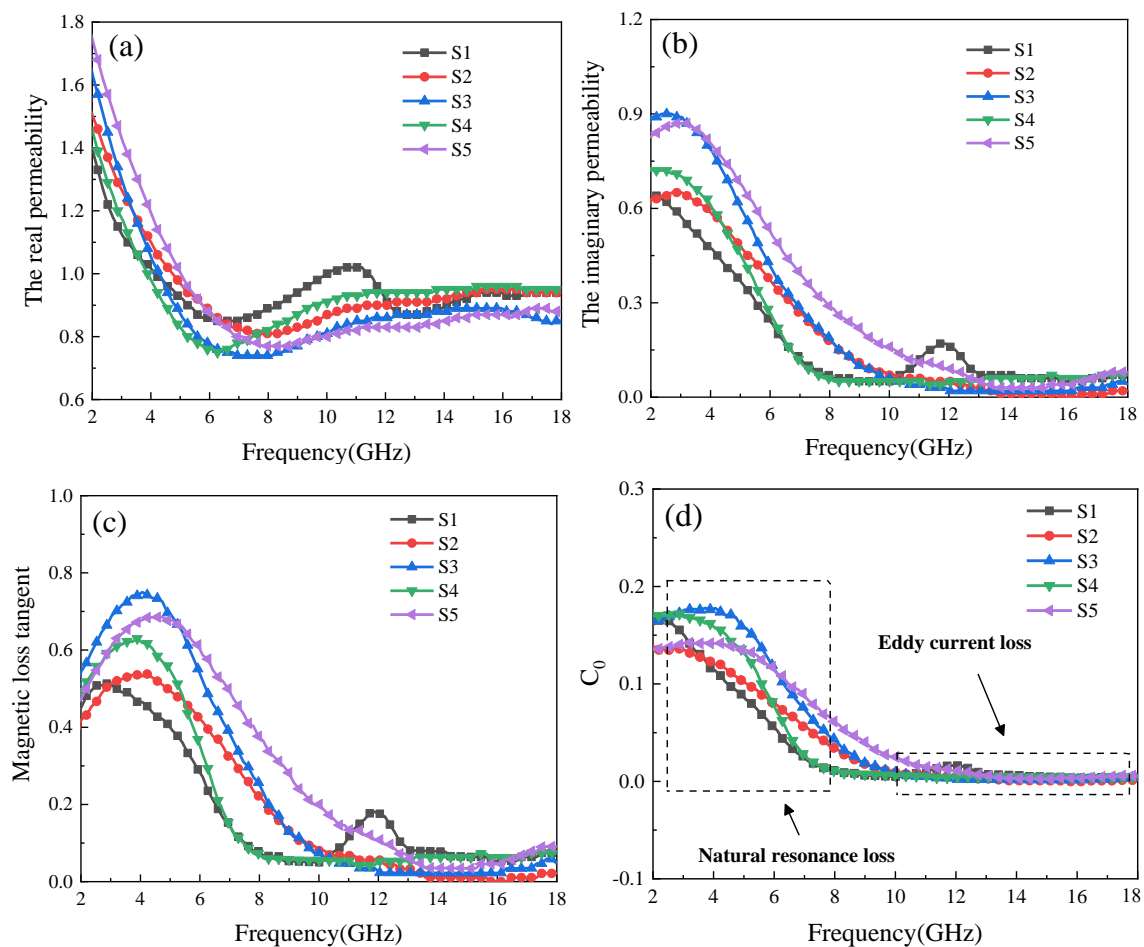
**Figure 5.** (**a**) The real part of permeability, (**b**) the imaginary part of permeability, (**c**) magnetic loss tangent, and (**d**) C_0 curves in the range of 2–18 GHz.

The energy of the electromagnetic wave is transferred to heat energy by dielectric loss and magnetic loss as the electromagnetic wave enters into the absorber. The attenuation constant α determines the capability attenuation characteristics of materials to attenuate the electromagnetic wave, which can be expressed by the following formula [30–32];

$$\alpha = \frac{\sqrt{2}\pi f}{c} \sqrt{\mu'' \varepsilon'' - \mu' \varepsilon' + \sqrt{(\mu'' \varepsilon'' - \mu' \varepsilon')^2 + (\varepsilon' \mu'' + \varepsilon'' \mu')^2}} \tag{6}$$

In Formula (6), c and f represent the velocity of light and frequency, respectively. The attenuation coefficient α of different Fe_3O_4 samples in the frequency range of 2–18 GHz can be visually expressed by the contour plot map, as shown in Figure 6. The result shows that the attenuation ability of Fe_3O_4 to electromagnetic wave is mainly reflected in the low and high frequency bands, while the attenuation ability of Fe_3O_4 to the medium frequency band is weak. With increasing reaction time, the attenuation coefficient of the intermediate frequency band decreases gradually, reaches the minimum at 20 h (S4), and increases after the sphere ruptures at 24 h (S5). To study the attenuation ability of different samples in each work frequency bands, the integral values of α in each band are calculated. The specific results are shown in Table 3. When the reaction time is 8–16 h (S1–S3), the total integral value of α in the range of 2–18 GHz increases, then decreases sharply (S4). When the sphere ruptures, the total integral value rises immediately. Based on the above calculation results, the electromagnetic wave absorption capacity of the samples can be arranged in the following order: S5 > S3 > S2 > S1 > S4.
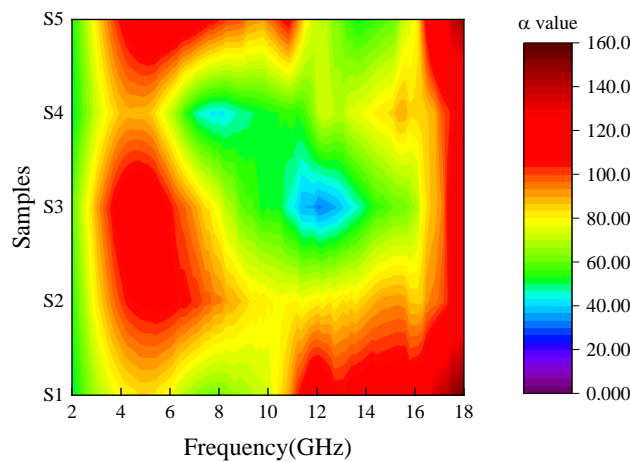
Figure 6. Attenuation coefficient contour map of Fe_3O_4 samples in the range of 2–18 GHz.

Table 3. Integral values of attenuation coefficients of Fe_3O_4 samples at different bands.

| Sample	S Band	C Band	X Band	Ku Band	Total
S1	90.09	125.41	131.85	383.46	730.81
S2	101.57	214.96	122.20	459.66	898.39
S3	182.44	382.66	90.10	245.88	901.08
S4	111.83	173.48	99.50	201.79	586.60
S5	154.03	415.93	178.51	184.52	932.99

On the basis of the complex permittivity and complex permeability data, the reflection loss (R_L) of Fe_3O_4 can be deduced from the transmission line theory [33]:

$$R_L = 20lg\left|\frac{Z_{in} - Z_0}{Z_{in} + Z_0}\right| \tag{7}$$

$$Z_{in} = \sqrt{\frac{\mu_r}{\varepsilon_r}}\tanh\left|j\frac{2\pi df}{c}\sqrt{\mu_r\varepsilon_r}\right| \tag{8}$$

Among them, Z_{in} stands for the input impedance of absorbing material, Z_0 is the impedance of free space, c is the speed of light in vacuum, d is the thickness of absorber, and f represents microwave frequency. Based on the above formulas, R_L can be simulated as the thickness is in the range of 0–10 mm and the frequency is 2–18 GHz, as depicted in Figure 7a–e. The absorption peak of the sample moves to low frequency gradually as the thickness increases, which can be explained by the equation [34]: $f = c/2\pi d\mu''$, where f represents the optimal matching frequency, d is the optimal matching thickness. Therefore, the absorption band can be adjusted by changing the thickness of Fe_3O_4 to meet the actual needs. Moreover, when the thickness of the sample exceeds a certain value (S1–4.8 mm, S2–4.3 mm, S3–3.8 mm, S4–4.8 mm, S5–4.2 mm), there are absorption peaks at both low and high frequencies, which indicates that Fe_3O_4 is promising as a low frequency and high frequency compatible microwave absorbing material. In addition, R_L is very sensitive to the change of thickness and can produce very strong reflection loss at a specific thickness. That can be explained by a quarter-wavelength model [35]:

$$t_m = \frac{nc}{4f_m\sqrt{|\varepsilon_r||\mu_r|}}; \; n = 1, 3, 5, \ldots \tag{9}$$
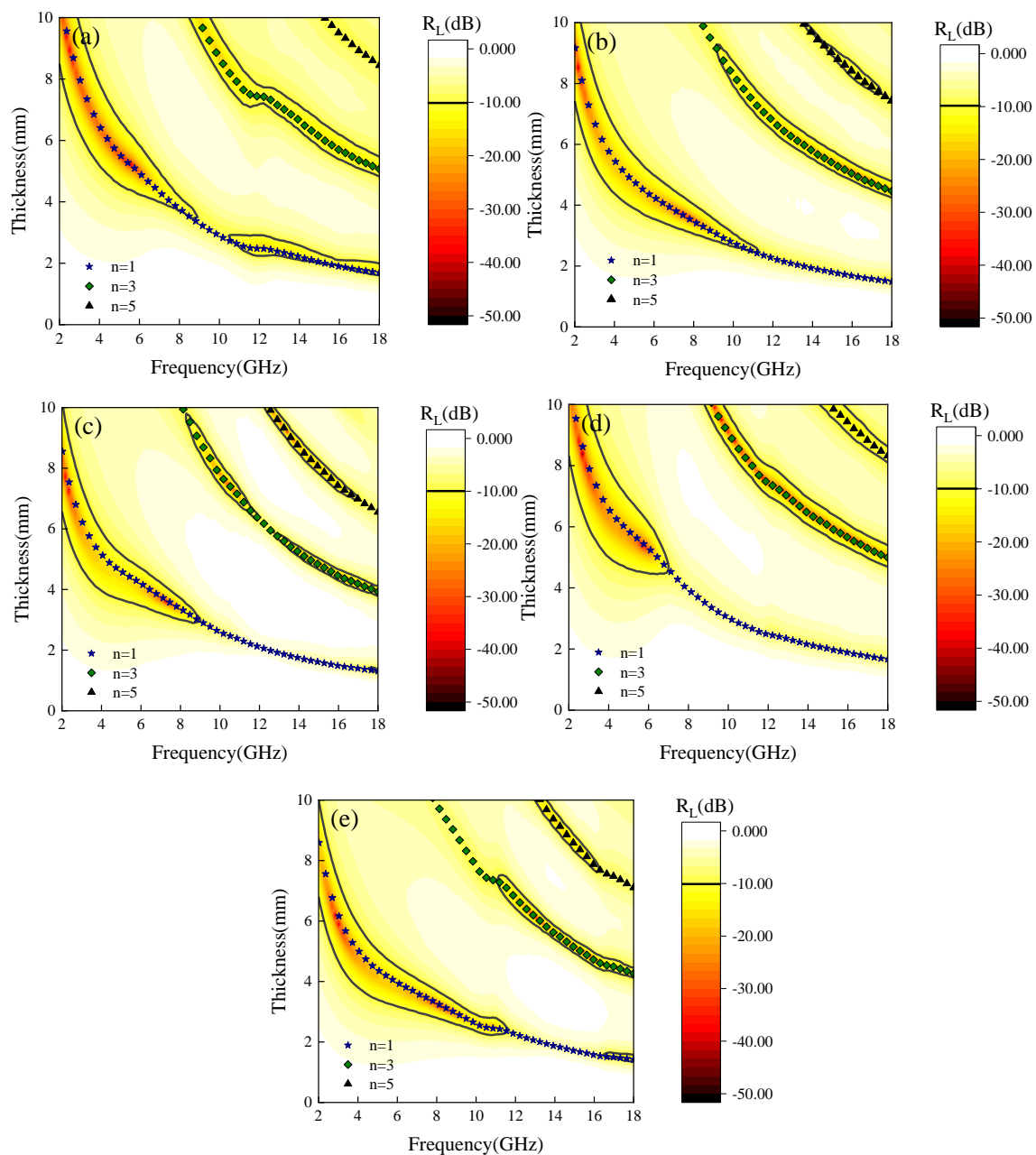
Figure 7. Fe$_3$O$_4$ reflection loss diagrams: (**a**) S1, (**b**) S2, (**c**) S3, (**d**) S4 and (**e**) S5.

Where $|\varepsilon_r|$ and $|\mu_r|$ are the modulus of ε_r and μ_r at f_m, respectively. If the thickness of the absorber is equal to the calculated t_m, the interference effect will occur, and the electromagnetic wave will be attenuated greatly. When n = 1, 3 and 5, the frequency dependence of t_m is calculated and plotted on the contour maps of S1–S5 in Figure 7. It can be observed that almost all the points of $R_{L\,(min)}$ on the curves of t_m. Thus, we can judge that the absorption peaks of Fe$_3$O$_4$ samples are aroused by thickness resonance to the specific frequency microwave.

As the thickness of the sample increases, the resonance thicknesses are satisfied, with the quarter-wavelength model appearing in turn, which are 3.2 mm—S5, 3.6 mm—S3, 3.7 mm—S2, 5.2 mm—S1 and 5.4 mm—S4, respectively. The order is consistent with the order of attenuation ability mentioned above and the R_L at resonance thickness are shown in Figure 8a. The absorption band of samples at the resonance thickness is mainly concentrated at low frequency, it might be related to the strong natural resonance loss at low frequency. Additionally, $R_{L\,(min)}$ of each sample can approach −40 dB, which is equivalent to 99.99% of the electromagnetic wave energy absorbed,

indicating that Fe_3O_4 possesses great potential as an excellent low-frequency microwave absorption material. The normalized characteristic impedance Z is a key parameter in reducing the reflection of the electromagnetic wave, which can be expressed by the following equation [36]:

$$Z = \frac{Z_{in}}{Z_0} = \sqrt{\frac{\mu_r}{\varepsilon_r}} \tanh \left| j \frac{2\pi d f}{c} \sqrt{\mu_r \varepsilon_r} \right| \tag{10}$$
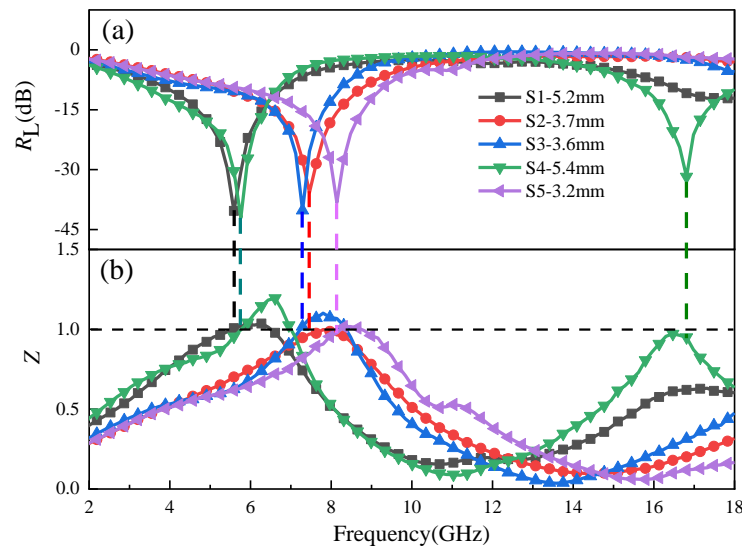

Figure 8. (**a**) The R_L and (**b**) Z of Fe_3O_4 samples at resonance thickness.

Input impedance Z_{in} should be equal to the free space impedance Z_0, so that the electromagnetic wave can enter into the absorber completely and can be totally attenuated completely; thus, Z should be as close as possible to 1. As shown in Figure 8b, at the optimum thickness and frequency of the sample, the Z values corresponding to the loss peaks are closed to 1, indicating that they are well matched with the free space impedance. In addition, by comparing the attenuation ability, the relationship between resonance thickness and Z, it is easy to draw the conclusion that the impedance matching of Fe_3O_4 hollow spheres can be achieved in a thinner case when the attenuation ability is strong.

4. Conclusions

Fe_3O_4 hollow spheres were fabricated with different reaction times by Ostwald ripening process. The microstructure and electromagnetic properties have been investigated systemically. Fe_3O_4 spheres all have hollow structure at different reaction times ranging from 8 h to 24 h, the size of Fe_3O_4 spheres remains at about 500 nm in diameter. The grain size and hollowness of Fe_3O_4 spheres increase as the reaction time. Fe_3O_4 hollow spheres break down as the reaction time reaches 24 h. With increasing in hollowness, the electromagnetic wave attenuation ability of Fe_3O_4 spheres increases first and then decreases, and increases sharply after the spheres finally break down. There is an obvious effect on the dielectric and magnetic properties of Fe_3O_4 spheres with different morphologies, resulting in a significant difference in the attenuation ability of different samples to electromagnetic waves. The electromagnetic attenuation ability of Fe_3O_4 spheres is S5 > S3 > S2 > S1 > S4. Sample with strong attenuation ability can achieve impedance matching preferentially with an increase in thickness. In addition, Fe_3O_4 hollow nanospheres exhibit good microwave absorption properties due to the strong natural resonance loss and interference cancellation of electromagnetic wave. $R_{L\,(min)}$ can reach -40 dB as the thickness is only 3.2 mm and the reaction time is 24 h.

References

1. Duan, L.F.; Zhang, X.Y.; Yue, K.Q.; Wu, Y.; Zhuang, J.; Lv, W. Synthesis and electrochemical property of $LiMn_2O_4$ porous hollow nanofiber as cathode for lithium-ion batteries. *Nanoscale Res. Lett.* **2017**, *12*, 109. [CrossRef] [PubMed]

2. Qi, X.H.; Zheng, W.J.; He, G.H.; Tian, T.F.; Du, N.X.; Wang, L. $NiCo_2O_4$ hollow microspheres with tunable numbers and thickness of shell for supercapacitors. *Chem. Eng. J.* **2017**, *309*, 426–434. [CrossRef]

3. Chen, P.; Cui, B.; Cui, X.R.; Zhao, W.W.; Bu, Y.M.; Wang, Y.Y. A microwave-triggered controllable drug delivery system based on hollow-mesoporous cobalt ferrite magnetic nanoparticles. *J. Alloys Compd.* **2017**, *699*, 526–533. [CrossRef]

4. Wu, Z.C.; Li, W.P.; Luo, C.H.; Su, C.H.; Ye, C.S. Rattle-type Fe_3O_4@CuS developed to conduct magnetically Guided photoinduced hyperthermia at first and second NIR biological windows. *Adv. Funct. Mater.* **2015**, *25*, 6527–6537. [CrossRef]

5. Lai, X.Y.; Li, J.; Korgel, B.A.; Dong, Z.H.; Li, Z.M.; Su, F.B.; Du, J.; Wang, D. General synthesis and gas-sensing properties of multiple-shell metal oxide hollow microspheres. *Angew. Chem.* **2011**, *50*, 2738–2741. [CrossRef] [PubMed]

6. Owens, F.J. Ferromagnetic resonance of magnetic field oriented Fe_3O_4 nanoparticles in frozen ferrofluids. *J. Phys. Chem. Solids* **2003**, *64*, 2289–2292. [CrossRef]

7. Zhai, C.X.; Du, N.; Zhang, H.; Yang, D.R. Cobalt-iron cyanide hollow cubes: Three-dimensional self-assembly and magnetic properties. *J. Alloys Compd.* **2011**, *509*, 8382–8386. [CrossRef]

8. Niu, K.Y.; Park, J.W.; Zheng, H.M.; Alivisatos, A.P. Revealing Bismuth Oxide Hollow Nanoparticle Formation by the Kirkendall Effect. *Nano Lett.* **2013**, *13*, 5715–5719. [CrossRef]

9. Zhao, B.; Guo, X.Q.; Zhou, Y.Y.; Su, T.T.; Ma, C.; Zhang, R. Constructing hierarchical hollow CuS microspheres via a galvanic replacement reaction and their use as wide-band microwave absorbers. *Cryst-EngComm* **2017**, *19*, 2178–2186. [CrossRef]

10. Jia, H.X.; Xing, H.L.; Ji, X.L.; Gao, S.T. Synergistic effect of hexagonal flake Co_3O_4@PANI core-shell composites with excellent microwave-absorbing properties. *J. Mater. Sci.-Mater. Electron.* **2019**, *30*, 1–10. [CrossRef]

11. Qiu, H.; Luo, X.; Wang, J.; Zhong, X.L.; Qi, S.H. Synthesis and characterization of ternary polyaniline/barium ferrite/reduced graphene oxide composite as microwave-absorbing material. *J. Electron. Mater.* **2019**, *48*, 1–9. [CrossRef]

12. Ji, P.C.; Xie, G.Z.; Xie, N.Y.; Li, J.; Chen, J.; Chen, J.W. Microwave absorbing properties of flaky carbonyl iron powder prepared by rod milling method. *J. Electron. Mater.* **2019**, *48*, 2495–2500. [CrossRef]

13. Micheli, D.; Pastore, R.; Delfini, A.; Giusti, A.; Vricella, A.; Santoni, F.; Marchetti, M.; Tolovhko, O.V.; Vasilyeva, E. Electromagnetic characterization of advanced nanostructured materials and multilayer design optimization for metrological and low radar observability applications. *Acta Astronaut.* **2017**, *134*, 33–40. [CrossRef]

14. Wang, H.Y.; Zhang, Y.L.; Wang, Q.Y.; Jia, C.W.; Cai, P.; Chen, G.; Dong, C.J.; Guan, H.T. Biomass carbon derived from pine nut shells decorated with NiO nanoflakes for enhanced microwave absorption properties. *RSC Adv.* **2019**, *9*, 9126–9135. [CrossRef]

15. Wang, Y.P.; Peng, Z.; Jiang, W. Controlled synthesis of Fe_3O_4@SnO_2/RGO nanocomposite for microwave absorption enhancement. *Ceram. Int.* **2016**, *42*, 10682–10689. [CrossRef]

16. Qiao, M.T.; Lei, X.F.; Ma, Y.; Tian, L.D.; Wang, W.B.; Su, K.H.; Zhang, Q.Y. Facile synthesis and enhanced electromagnetic microwave absorption performance for porous core-shell Fe_3O_4@MnO_2 composite microspheres with lightweight feature. *J. Alloys Compd.* **2017**, *693*, 432–439. [CrossRef]

17. Peng, S.; Sun, S. Synthesis and characterization of monodisperse hollow Fe_3O_4 nanoparticles. *Angew. Chem. Int. Ed.* **2010**, *46*, 4155–4158. [CrossRef] [PubMed]

18. Bin, Q.; Zhu, C.L.; Li, C.Y.; Zhang, X.T.; Chen, Y.J. Coupling hollow Fe_3O_4-Fe nanoparticles with graphene sheets for high-performance electromagnetic wave absorbing material. *ACS Appl. Mater. Interfaces* **2016**, *8*, 3730–3735.

19. Pastore, R.; Delfini, A.; Micheli, D.; Vricella, A.; Marchetti, M.; Santoni, F.; Piergentili, F. Carbon foam electromagnetic mm-wave absorption in reverberation chamber. *Carbon* **2019**, *144*, 63–71. [CrossRef]

20. Li, Z.W.; Yang, Z.H. Microwave absorption properties and mechanism for hollow Fe_3O_4 nanosphere composites. *J. Magn. Magn. Mater.* **2015**, *387*, 131–138. [CrossRef]

21. Sui, M.X.; Sun, X.D.; Lou, H.F.; Li, X.P.; Lv, X.L.; Gu, G.X. Synthesis of hollow Fe_3O_4 particles via one-step solvothermal approach for microwave absorption materials: Effect of reactant concentration, reaction temperature and reaction time. *J. Mater. Sci.-Mater. Electron.* **2018**, *29*, 7539–7550. [CrossRef]

22. Xu, H.L.; Shen, Y.; Bi, H.; Liang, W.F.; Yang, R.B. Preparation and microwave absorption properties of Fe_3O_4 hollow microspheres. *Ferroelectrics* **2012**, *435*, 98–103. [CrossRef]

23. Sarkar, D.; Mandal, M.; Mandal, K. Domain controlled magnetic and electric properties of variable sized magnetite nano-hollow spheres. *J. Appl. Phys.* **2012**, *112*, 06318. [CrossRef]

24. Zhao, S.Z.; Wu, H.Y.; Lin, S.; Tegus, O.; Asuha, S. Preparation of γ-Fe_2O_3, nanopowders by direct thermal decomposition of Fe-urea complex: reaction mechanism and magnetic properties. *J. Mater. Sci.* **2009**, *44*, 926–930. [CrossRef]

25. Lee, J.; Isobe, T.; Senna, M. Preparation of Ultrafine Fe_3O_4 Particles by Precipitation in the Presence of PVA at High pH. *J. Colloid Interface Sci.* **1996**, *177*, 490–494. [CrossRef]

26. Cole, K.S.; Cole, R.H. Dispersion and Absorption in Dielectrics I. Alternating Current Characteristics. *J. Chem. Phys.* **1941**, *9*, 341–351. [CrossRef]

27. Li, N.; Huang, G.W.; Li, Y.Q.; Xiao, H.M.; Feng, O.P.; Hu, N.; Fu, S.Y. Enhanced microwave absorption performance of coated carbon nanotubes by optimizing the Fe_3O_4 nanocoating structure. *ACS Appl. Mater. Interfaces* **2017**, *9*, 2973–2983. [CrossRef] [PubMed]

28. Meng, F.B.; Wang, H.G.; Huang, F.; Guo, Y.F.; Wang, Z.Y.; Hui, D.; Zhou, Z.W. Graphene-based microwave absorbing composites: A review and prospective. *Compos. Part B-Eng.* **2018**, *137*, 260–277. [CrossRef]

29. Lu, M.M.; Cao, M.S.; Chen, Y.H.; Cao, W.Q.; Liu, J.; Shi, H.L.; Zhang, D.Q.; Wang, W.Z.; Yuan, J. Multiscale assembly of grape-like ferroferric oxide and carbon nanotubes: A smart absorber prototype varying temperature to tune intensities. *ACS Appl. Mater. Interfaces* **2015**, *7*, 19408–19415. [CrossRef]

30. Liu, X.G.; Ou, Z.Q.; Geng, D.Y.; Xie, Z.G.; Zhang, Z.D.; Han, Z. Enhanced natural resonance and attenuation properties in superparamagnetic graphite-coated $FeNi_3$ nanocapsules. *J. Phys. D Appl. Phys.* **2009**, *42*, 155004–155009. [CrossRef]

31. Shi, G.M.; Zhang, B.; Wang, X.L.; Fu, Y.H. Enhanced microwave absorption properties of core double-shell type Fe@C@$BaTiO_3$ nanocapsules. *J. Alloys Compd.* **2016**, *655*, 130–137. [CrossRef]

32. Jazirehpour, M.; Ebrahimi, S. Effect of aspect ratio on dielectric, magnetic, percolative and microwave absorption properties of magnetite nanoparticles. *J. Alloys Compd.* **2015**, *638*, 188–196. [CrossRef]

33. Naito, Y.; Suetake, K. Application of ferrite to electromagnetic wave absorber and its characteristics. *IEEE Trans. Microw. Theory* **1971**, *19*, 65–72. [CrossRef]

34. Qin, F.X.; Brosseau, C. A review and analysis of microwave absorption in polymer composites filled with carbonaceous particles. *J. Appl. Phys.* **2012**, *111*, 061301–061324. [CrossRef]

35. Du, Y.C.; Liu, W.W.; Qiang, R.; Han, X.J.; Ma, J.; Xu, P.; Wang, Y. Shell thickness-dependent microwave absorption of core-shell Fe_3O_4@C composites. *ACS Appl. Mater. Interfaces* **2014**, *6*, 12997–13006. [CrossRef] [PubMed]

36. Gao, X.B.; Zhang, K.C.; Zhang, Q.; Li, C.W.; Wang, Y.; Chen, X.F. Porous corn-like Fe_3O_4 nanosheets decorated fluffy graphene nanocomposites and their enhanced microwave absorption properties. *J. Mater. Sci.-Mater. Electron.* **2018**, *29*, 12178–12186. [CrossRef]